Breakup of Thin Liquid Filaments on Partially Wetting Substrates: from Micrometric to Nanometric Scales

Javier A. Diez & Alejandro G. González

Brazilian Journal of Physics

ISSN 0103-9733
Volume 46
Number 2

Braz J Phys (2016) 46:225-237
DOI 10.1007/s13538-015-0392-1

Springer

Braz J Phys (2016) 46:225–237
DOI 10.1007/s13538-015-0392-1

SOCIEDADE BRASILEIRA DE FÍSICA

GENERAL AND APPLIED PHYSICS

Breakup of Thin Liquid Filaments on Partially Wetting Substrates: from Micrometric to Nanometric Scales

Javier A. Diez[1] · **Alejandro G. González**[1]

Received: 19 October 2015 / Published online: 30 December 2015

Abstract We present theoretical and experimental results regarding the instability of a thin liquid film in the form a long filament sitted on a solid substrate. We consider this problem in two different scenarios, namely, at submillimetric and nanometric scales, and we study their free surface instability. In the first scale, we take into account the effects due to surface tension and gravity, while in the smaller scale, we add intermolecular interaction and neglect gravity. The flows are modeled within the long wave approximation, which leads to a nonlinear fourth-order differential equation for the fluid thickness. This model equation also includes the partial wetting condition between the liquid and the solid. In the theoretical models, we analyze the linear stability of the equilibrium configurations. The linear stability analyses lead to eigenvalue problems that are solved using pseudo spectral methods in the submillimetric case, and finite differences in the nanoscale. Whenever possible, the theoretical results are compared with experiments performed on a submillimetric scale (silicon oils on glass), as well as on nanometric scale (nickel films melted by laser irradiation on SiO2 substrates).

Keywords Thin liquid films · Instabilities · Surface tension · Disjoining pressure

✉ Javier A. Diez
jdiez@exa.unicen.edu.ar

Alejandro G. González
aggonzal@exa.unicen.edu.ar

[1] Instituto de Física Arroyo Seco (CIFICEN-CONICET), Universidad Nacional del Centro de la Provincia de Buenos Aires, Pinto 399, 7000, Tandil, Argentina

1 Introduction

The process formation of liquid particles appears in different contexts from macroscopic (submillimetric or micron scale) to nanometric scales. In this paper, we shall discuss the instability processes that occur when a liquid is deposited on a substrate with a given geometry in both macro and microscales. Here, we focus on thin structures with the form of a long filament.

There is presently much interest in the production of nanoparticles, the main reason being that some important material properties, such as magnetic moment [1], ionization potential, surface tension [2], and melting point [3] are drastically affected by metallic nanoparticles size in the sub-20-nm diameter range. Some applications stand to benefit from these size-dependent properties [4, 5]. Since the pattern formed by these nanoparticles on substrates plays a crucial role, some physical-based methods result more convenient than chemical ones [6]. The latter are very efficient to form drops with a precise radius (or a specific range of radii), but fail to produce a desired arrangement. Instead, the physical methods are more appropriate to produce a defined pattern.

One example of the use of nanodrops in applications is the combination of the resonant plasmonic properties of metallic nanoparticles within the thin-films photovoltaic technology [7]. Plasmonic solar cells, where the silicon wafer is coated with silver nanoparticles, are emerging as promising candidates amongst many solar energy technologies. Another example is the controlled growth of semiconductor nanowires (particularly Si and Ge) starting from a substrate, by chemical vapor deposition (CVD). Its preparation is a key factor in controlling the morphology of the resulting growth. Parallel vertical nanowires grown epitaxially from the substrate are of particular interest for

manufacturable electronic, optical, and some photovoltaic applications. Most of the emerging physical methods (developed to pattern drops on a substrate as integrated processes) include lithographic methods. Here, we will focus instead on the pulsed laser induced dewetting (PLiD) processes as an alternative. In this context, thin film dewetting has recently attracted much interest as a way to yield a spatially correlated metal particle network on a surface [8, 9]. Surface waves evolving spontaneously on liquid films are either stable, leading to a smooth film, or unstable, leading to film fragmentation and formation of particles. While in the nanometric scale, this process involves a complex interplay between the laser melting (laser absorption depth and metal heating/melting) and the resultant liquid surface energies and viscosity, a simpler experiment can be used as a benchmark of the theories and models: submillimetric scale systems using silicon oils instead of melted metals. Thus, we study here the macroscopic case of a long filament to understand the main fluid dynamics features, in order to shed some light on the analogous instability issues in the nanometric scale.

2 Submillimetric Range

The aim of this section is to discuss the instability of a thin liquid filament placed on a substrate with characteristic transverse lengths in the range of a few millimeters down to some micrometers (i.e., in a macroscopic scale). In this case, both surface tension and gravitational forces must be taken into account. First, we describe the experimental techniques used [10], and then we carry out the theoretical treatment of the instability. At the end of this section, we compare the theoretical predictions with the experimental data.

2.1 Experiments with Silicon Oils

The substrate used in the experiments is a microscope slide coated with a fluorinated solution (EGC-1700 of 3M) by dip coating under controlled speed ($\approx 5\ mm/s$). This coating ensures that the substrate is partially wetted by the silicon oil (polydimethylsiloxane, PDMS). In order to generate the initial condition (filament), we start with a vertical jet of PDMS flowing down from a small nozzle at the bottom of a vessel filled with the silicon oil [11] (viscosity $\mu = 20$ Poise, density $\rho = 0.96\,\mathrm{g/cm^3}$, and surface tension $\gamma = 21\,dyn/cm$). The diameter, d (0.3–1 mm), of the resulting jet, and its cross section A, are highly reproducible and can be regulated by varying the nozzle diameter, the height of the oil in the vessel, and the fluid viscosity.

The filament is captured from the jet on a substrate by performing suitable rotations of its frame before reaching the final horizontal position. All these movements take about from 1 to 2 s, i.e. a time interval which is very short compared to the time scale of the experiment. This experimental procedure yields a fluid filament of uniform width, w, with parallel and straight contact lines, so that the initial configuration has a constant cross-sectional area along the filament axis [11]. The wettability of PDMS on the coated glass is characterized by measuring the static contact angle, θ_0, of a single circular drop at rest on a horizontal substrate. Since the drop is placed from the tip of a syringe, the drop edge corresponds to an advancing contact lines till it reaches the maximum radius.

Once the filament is on the substrate, the main perturbations are localized at its extremes, while the rest of it is in equilibrium. Then, the extremes begin to dewet along the filament axis, where a bulge is developed and whose size increases as the reduction of the length of the filament goes on. Meanwhile, the width of the neck connecting the bulge and the filament decreases until it finally pinches off and a drop detaches at each extreme. As the axial dewetting process continues, successive bulges and neck pinch-offs give place to a near equidistant linear array of drops (see Fig. 1).

In order to probe the evolution of the neck region as well as to observe the shape of the contact line along the whole filament, a schlieren technique is used. In addition, this method allows us to ascertain that the initial maximum thickness is uniform, which ensures that there is no externally imposed characteristic wavelength within the experimental error. A typical pinch-off process is shown in Fig. 2, where we can see a short region of the uniform filament (on the left) and half of the bulge/drop (on the right). The width of the neck decreases until it breaks up,

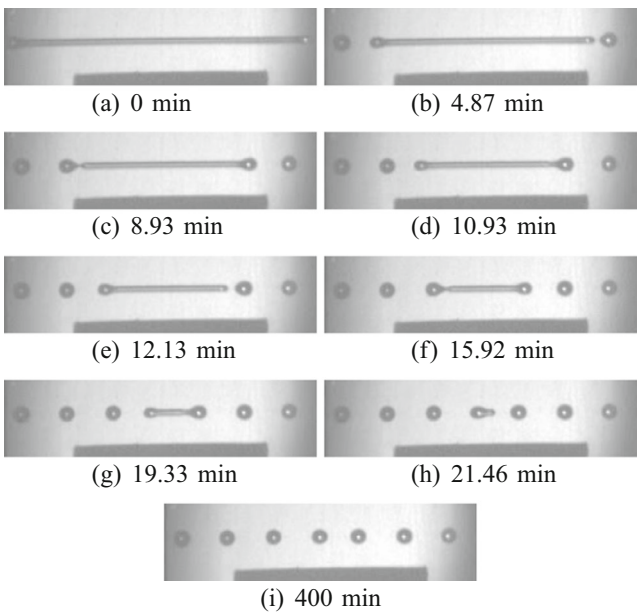

Fig. 1 Evolution of the system and formation of primary drops [10]. The *black segment* corresponds to 4.2 cm

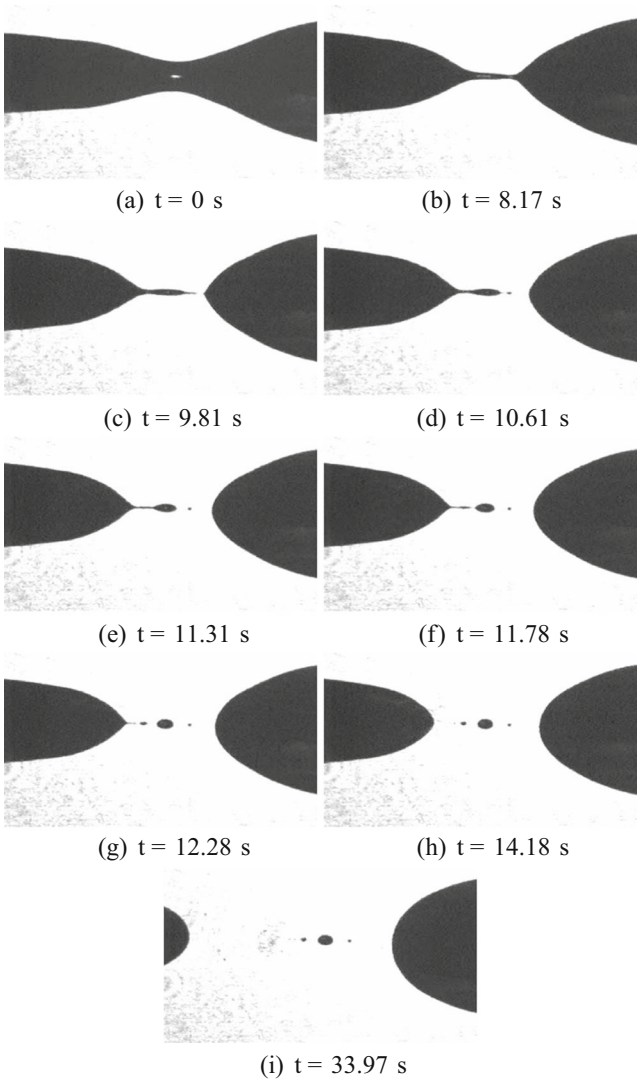

Fig. 2 Close up of the pinch off of a filament and generation of secondary drops [10]. **a** Formation of the neck, **b** advanced stage of the pinch off process, **c** first break up of the neck, **d** detachment of the tertiary droplet on the right from the secondary one, **e** buildup of the secondary drop, **f** detachment of the secondary drop from the left bridge, **g** formation of the tertiary droplet on the left by the breakup of the remaining bridge, **h** dewetting of the main strip, and **i** final shape of the primary drop and further dewetting of the strip

so that the bulge evolves into a detached drop. This process is not symmetric (it occurs first on the drop side), and it originates secondary droplets, as well as tertiary smaller droplets. Furthermore, we have been able to detect quaternary drops in several cases. This type of breakup process is repeated until an array of quasi-equidistant primary drops is achieved (Fig. 1). All drops reach an equilibrium state since no detectable change in shape is observed after several days. Note that the formation of each primary drop involves two processes: the breakup process and the receding motion of the bulges. The duration of the former is of the order of tens of seconds (see Fig. 2) while that of the latter is of the order of some minutes, depending on the width of the original filament.

2.2 Long Wave Approximation with Slipping and Gravity

In the study of thin film flows on solid substrates, the evolution of the fluid thickness, h, is typically described under the framework of the long wave approximation or lubrication theory (see e.g. [12]). This approach allows to reduce Navier–Stokes equations to a single nonlinear partial differential equation for h.

We note that although lubrication theory is strictly valid only in problems characterized by vanishing free surface slopes, it has been used commonly in partial wetting conditions, therefore in situations in which the contact angle is not necessarily small [13–15] (see also [16–19] for further discussion regarding involved issues). This approach has been justified in part by some works that show that even in the case of large contact angles, only relatively small deviations from more complete models result. For example, [20] compares the solutions for the cross section of a filament flowing down a plane obtained by solving the complete Navier-Stokes equation with the predictions of the lubrication approximation (see their Table I). For a contact angle of 30°, they find that the differences between the two approaches related with the shape of the free surface are of the order of a few percents.

Although the accuracy of the lubrication approximation is not so good regarding the details of the velocity field, they find that these velocity differences cancel out when the total flux along the filament is computed. The issue of appropriateness of the use of the lubrication approximation was also discussed earlier [21]. In that work, it was shown that there are some differences in the free surface slope between lubrication theory and Stokes formulation, but only very close to the contact line. Another concern regarding the use of the lubrication approximation is that one typically (as we do here) approximates the curvature of the free surface by h_{xx} , where x is an in-plane coordinate. This issue was considered in [22], where it is shown that the use of the complete nonlinear curvature yields only a few percent difference (see, e.g. Fig. 2b in [22]). There have been also some attempts [23, 24] to improve the typical lubrication approximation approach. These works show that including a correction factor to the flux term in the continuity equation extends the limits of its validity.

Therefore, it may be appropriate to implement these improvements when precise quantitative results are desired. Here, where we are mainly concerned with the basic mechanisms involved in the dewetting and breakup processes, we expect that the standard lubrication approach is sufficient. The resulting equation for the fluid thickness, h, are shown

below in (11) and (43) for the macroscopic and nanometric approaches, respectively (see, e.g., [12, 25, 26]). The van der Waals forces are included in the formulation of a lubrication model via disjoining pressure (see, e.g., Appendix A in [27])

2.2.1 Static Solution

The governing equation for the thickness profile of the static filament is obtained by considering the fact that velocity field vanishes everywhere. Therefore, the *dimensionless* balance between the pressure and gravitational forces can be written as,

$$0 = -\nabla p - \hat{\mathbf{z}}. \tag{1}$$

Here, the spatial variables (x, y, and z) are in units of the length scale

$$L_1 = a, \tag{2}$$

where $a = \sqrt{\gamma/(\rho g)}$ is the capillary length, with g the gravity (e.g., we have $a = 0.145$ cm for PDMS). Then, the pressure p is in units of γ/a.

By introducing the Laplace pressure boundary condition for small slopes, we have, $p = -h_0''$ at the filament free surface, $z = h_0(x)$ (y-direction is along the filament). Then, integration of (1) yields

$$h_0'' - h_0 + p_0 = 0, \tag{3}$$

where the constant, p_0, is the value of the fluid pressure inside the filament. The boundary conditions for (3) are

$$h_0 = 0, \; h_0' = \tan\theta_0, \tag{4}$$

at $x = s_0$, which is the position of the leading (front) contact line of the static filament. Here, we choose $x = 0$ as the middle point of the filament so that $s_0 = w/2$, where w is the filament width. The solution of (3) which satisfies (4) can be found analytically as [28]

$$h_0(x) = p_0\left[1 - \frac{\cosh x}{\cosh s_0}\right]. \tag{5}$$

The pressure p_0 is obtained from the condition of constant area cross section

$$A = \int_{-s_0}^{s_0} h_0(x)dx \tag{6}$$

as

$$p_0 = \frac{A/2}{s_0 - \tanh s_0}. \tag{7}$$

In order to find s_0, we employ the contact angle conditions, (4), so that

$$\tan\theta_0 = p_0 \tanh s_0, \tag{8}$$

and then corresponding value of s_0 is then given by

$$\frac{2\tan\theta_0}{A} = \frac{\tanh s_0}{s_0 - \tanh s_0}, \tag{9}$$

which is solved numerically with given values of A and θ_0.

2.2.2 Linear Stability Analysis (LSA)

Considering stability of the filament leads to the issue of moving contact lines. Here, we resort to the slip model to regularize the well-known singularity along these lines [29]. In this context, instead of the no-slip condition of zero velocity parallel to the substrate, i.e., $v_x = 0$ at $z = 0$, we use the Navier boundary condition

$$v_x = \frac{\ell}{3}\frac{\partial v_x}{\partial z} \tag{10}$$

to allow the fluid to slip on the substrate, where ℓ is the slipping length in units of a. Therefore, under the usual assumptions of the lubrication theory, the governing equation for the thickness $h(x, y, t)$ obeys the following *dimensionless* fourth-order nonlinear partial differential equation [30, 31]

$$\frac{\partial h}{\partial t} + \nabla\cdot\left[h^2(h+\ell)\nabla\left(\nabla^2 h - h\right)\right] = 0, \tag{11}$$

where time t is in units of

$$T_1 = \frac{3\mu a}{\gamma}. \tag{12}$$

In (11), the first term in the square brackets stands for surface tension forces, while the second one represents gravity force. The conditions at the boundaries of the filament (contact lines) are now

$$h = 0, \quad \text{at} \quad x = s_l(y,t) \text{ and } \quad x = s_r(y,t), \tag{13}$$

where $s_l < 0$ ($s_r > 0$) is the position of the left (right) contact line of the filament. Since the initially straight contact lines may become corrugated during the drop motion, the slopes at the front and back boundaries are given by

$$\left.\frac{\partial h}{\partial x}\right|_{x=s_{l,r}}\left[1 + \left(\frac{\partial s_{l,r}}{\partial y}\right)^2\right]^{-1/2} = \mp\tan\theta_0, \tag{14}$$

where we assume that the amplitude of the corrugation is small, so that $\partial h/\partial y \ll 1$. Note that by putting $\ell = 0$ and ignoring y and t dependence in (11), (13) and (14), we recover the equations describing the static solution, $h_0(x)$.

In order to analyze the linear stability of the equilibrium static solution, we perform a linear modal analysis of (11). Thus, we perturb the thickness $h(x, y, t)$ and the positions of the contact lines with undulations of wavelength λ along the filament as

$$h(x,y,t) = h_0(x) + \epsilon\,\Phi(x)\cos(ky)\,e^{\omega t}, \tag{15}$$

$$s_l(y,t) = -s_0 + \epsilon\,\xi_l\cos(ky)\,e^{\omega t}, \tag{16}$$

$$s_r(y,t) = s_0 + \epsilon\,\xi_r\cos(ky)\,e^{\omega t},, \tag{17}$$

where $k = 2\pi/\lambda$ is the wavenumber. Substituting (15) into (11), we formulate the following eigenvalue problem,

$$\mathcal{L}\Phi = -\omega\,\Phi. \tag{18}$$

Here, $\mathcal{L}$ is a linear operator defined in compact form by

$$\begin{aligned}\mathcal{L}\Phi \;=\; & H_0\left(D^2-k^2\right)\left(D^2-k^2-1\right)\Phi \\ & +DH_0\left(D^2-k^2-1\right)D\Phi,\end{aligned} \tag{19}$$

where $D = d/dx$ and $H_0 = h_0^2(h_0+\ell)$. This expression can be expanded as

$$\begin{aligned}\mathcal{L}\Phi \;=\; & c_4(x)\Phi_{xxxx}+c_3(x)\Phi_{xxx}+c_2(x)\Phi_{xx}+c_1(x)\Phi_x \\ & +c_0(x)\Phi,\end{aligned} \tag{20}$$

where the coefficients $c_i(x)$ $(i = 0, ..., 4)$ are given by

$$\begin{aligned} c_4(x) &= H_0, \qquad c_3(x) = DH_0, \qquad c_2(x) = -\left(1+2k^2\right)H_0, \\ c_1(x) &= -\left(1+k^2\right)DH_0, \qquad c_0(x) = k^2\left(1+k^2\right)H_0. \end{aligned} \tag{21}$$

The linearized forms of the boundary conditions (13) and (14) yield

$$\Phi(-s_0)+\xi_r h_0'(-s_0) = 0, \qquad \xi_r h_0''(-s_0)+\Phi'(-s_0) = 0, \tag{22}$$

$$\Phi(s_0)+\xi_l h_0'(s_0) = 0, \qquad -\xi_l h_0''(s)-\Phi'(s_0) = 0. \tag{23}$$

From the known values of the derivatives of h_0 at the boundaries, the unknown amplitudes, $\xi_{l,r}$, can be eliminated from these conditions, which are replaced by

$$\Phi'(\pm s_0) = \frac{h_0''(\pm s_0)}{h_0'(\pm s_0)}\Phi(\pm s_0) = \kappa^{\pm}(s_0)\Phi(\pm s_0). \tag{24}$$

These boundary conditions now allow to solve the eigenvalue problem, (18), and find the eigenvalues, ω (the growth rates of the modes k). Although the equation to be solved is linear, it is fourth order with variable coefficients, so that its solution can only be found by resorting to numerical techniques. However, before solving this eigenvalue problem, we first discuss the marginal stability of the problem.

The neutral solution of (18) with $\omega = 0$ satisfies $(D^2 - k_c^2 - 1)\Phi = 0$ (see (19)), giving the following eigenfunction corresponding to marginally stable state

$$\Phi(x) = C_1\cosh\tilde{k}_c x + C_2\sinh\tilde{k}_c x, \tag{25}$$

where $\tilde{k}_c = \sqrt{k_c^2+1}$. Note that, as expected, this solution does not depend on the slip length, ℓ, since no motion of the contact line is required to describe the marginal stability. By inserting this expression into the boundary conditions, (24), we obtain a system of equations for C_1 and C_2. Since the eigenfunctions are unknown up to a multiplicative constant, we take $C_1 = 1$ and, by eliminating C_2, we have

$$\tilde{k}_c\tanh\left(\tilde{k}_c s_0\right)\tanh(s_0) = 1, \tag{26}$$

which is coincident with Eq. (4.21) in [32], where a variational principle was used for its derivation. As mentioned above, the marginal stability results are independent of the slip length ℓ. However, there can be influence of ℓ on the most unstable wavenumber, since instability requires front motion.

The linear eigenvalue problem posed by the differential operator in (19) combined with the boundary condition (24) can be solved numerically for a given value of k. This is done by discretizing the differential equation, (20), using a Chebyshev pseudo-spectral approximation of the derivatives, subject to the boundary condition specified by (24). This method is easier to implement and more accurate in imposing the boundary conditions at the contact lines compared to usual finite differences. Moreover, the number of nodes required with the pseudo-spectral method to obtain converged solutions is much smaller than with a difference scheme, leading to a significant reduction in the computing time (from hours to seconds).

Thus, under the pseudo-spectral method, we write the solution of (20) as

$$\Phi(x) = \sum_{i=1}^{N}\beta_i\phi_{i-1}(x), \tag{27}$$

where $\phi_i(x)$ is an orthogonal base, and β_i are unknown spectral coefficients. By using the Gauss-Lobatto grid [33]

$$x_i = s\cos\left(\frac{\pi i}{N-1}\right), \quad i = 1, 2, ..., (N-2), \tag{28}$$

we generate a matrix of dimension $N-2$ and require that the residual of the differential equation vanishes at the interpolation points on the interior of the interval $(-s_0, s_0)$. We allocate the remaining two rows of the N dimensional matrix to impose the boundary conditions.

In order to satisfy these conditions, we perform a basis recombination of Chebyshev functions, $T_i(x/s_0)$. That is, we choose a simple linear combination of the original basis functions so that the new functions individually satisfy the boundary conditions. Thus, we use the base $\phi_i(x)$ defined by

$$\phi_i(x) = T_i(x/s_0)+a_i T_{i+1}(x/s_0)+b_i T_{i+2}(x/s_0), \tag{29}$$

where $T_i(x/s_0) = \cos(i\arccos x/s_0)$. By inserting $\phi_i(x)$ into (24), we obtain two linear equations for the unknowns a_i and b_i

$$\begin{aligned}\left[(i+1)^2+\tilde{\kappa}^-\right]a_i-\left[(i+2)^2+\tilde{\kappa}^-\right]b_i &= \tilde{\kappa}^-+i^2 \\ \left[(i+1)^2-\tilde{\kappa}^+\right]a_i+\left[(i+2)^2-\tilde{\kappa}^+\right]b_i &= \tilde{\kappa}^+-i^2\end{aligned}$$

which are easily solved in terms of i, and $\tilde{\kappa}^{\pm} = \kappa^{\pm}s$. Then, we pose the eigenvalue problem

$$U_{i,j}\beta_i = -\omega V_{i,j}\beta_i, \quad i, j = 1, 2, ..., (N-2) \tag{30}$$

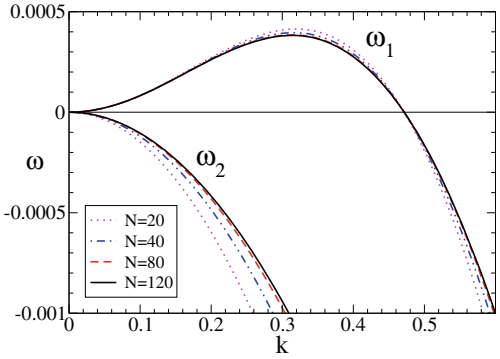

Fig. 3 Maximum eigenvalues obtained with Chebyshev pseudo spectral method versus wavenumber, k, with increasing number of spectral terms, showing convergence of the results. Here, we use $A = 1$, $\theta_0 = 30°$, and $\ell = 10^{-3}$

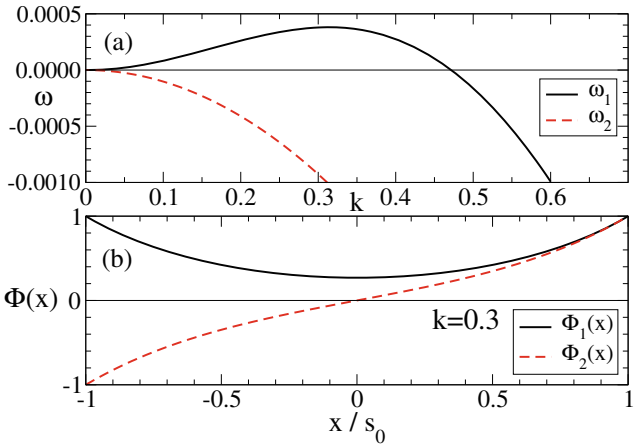

Fig. 4 **a** Dispersion curves and **b** eigenfunctions at $k = 0.3$ for the horizontal plane. The parameters are as in Fig. 3

where

$$U_{i,j} = \tilde{c}_4(x_i)\phi''''_{j-1}(x_i) + \tilde{c}_3(x_i)\phi'''_{j-1}(x_i) + \tilde{c}_2(x_i)\phi''_{j-1}(x_i) + \tilde{c}_1(x_i)\phi'_{j-1}(x_i) + \tilde{c}_0(x_i)\phi_{j-1}(x_i), \quad (31)$$

$$V_{i,j} = \phi_{j-1}(x_i), \quad (32)$$

and $\tilde{c}_i = s_0^i c_i$. For a given k, we find the largest eigenvalue, ω_1, with its corresponding eigenvector, β_i^1, which yields the eigenfunction $\Phi_1(x)$, as given by (27) for $\beta_i = \beta_i^1$. We find that a single eigenfunction correspond to each eigenvalue.

Figure 3 shows convergence of the results as N increases. Note that convergence is faster in the unstable branch, ω_1, compared to the stable one, ω_2. This is convenient since we are mainly interested in the growth rate of unstable modes. It should also be mentioned that the earlier work [31] focuses exclusively on this range, and the calculation of the growth rates is performed by means of an iterative method, in contrast to solving the complete eigenvalue problem as done here. We have verified that the present technique accurately reproduces the results reported in [31]. Additional calculations show that numerical convergence requires larger values of N for smaller ℓ. For example, for $\ell = 10^{-5}$, a convergence similar to that of Fig. 3 is achieved for $N = 640$.

We proceed by analyzing the dispersion curves. Figure 4 shows the two largest eigenvalues, $\omega_1(k)$ and $\omega_2(k)$, as well as the corresponding eigenfunctions for a selected value of k. Since these functions are defined up to a constant factor, we normalize them by their maximum value in the interval $[-1, 1]$ and choose the sign so that $\Phi(s_0) > 0$. With this convention, $\Phi_1(x)$ and $\Phi_2(x)$ correspond to symmetric (varicose) and antisymmetric (zig–zag) modes, respectively. These properties do not change along the corresponding branch. Note also that $|\Phi(x)|$ always reaches maximum value at the domain boundaries.

2.3 Comparison with Experiments: Silicon Oils

Figure 5 shows the final drop pattern after complete breakup of a filament with cross section $\widetilde{A} = 0.032a^2$ on a horizontal plane (see also [34]). Additional experiments with different A's were carried out, and the averaged distance between the drops was extracted.

Figure 6 summarizes the results for this average distance, shown as solid circles. These results can be now compared with the theoretical prediction from the linear stability analysis, λ_m, shown by the solid curve. Note the good agreement between the experimental data the theoretical curve for small areas ($A < 0.1$, in units of a^2).

The dispersion of the experimental data can be understood by recalling finite filament lengths effects. In fact, the wavelength of the mode of maximum growth rate, λ_m, may not fit an integer number of times in the length, L, of the filament. Thus, the system tends to select the closest possible spacing between drops that fits in the filament length and yields an integer number of identical drops, n_d. By taking this into account, we define a range of expected drops spacing that can have a positive or negative difference of at least

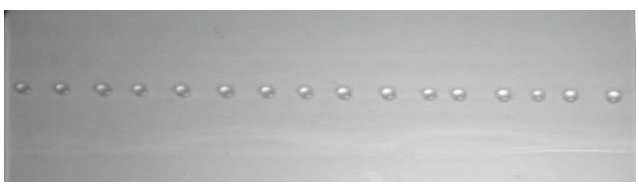

Fig. 5 Final drop configuration for a PDMS filament with cross section $\widetilde{A} = 0.0007\ cm^2 = 0.032a^2$ on a horizontal substrate, where $\theta_0 = 17° \pm 1°$

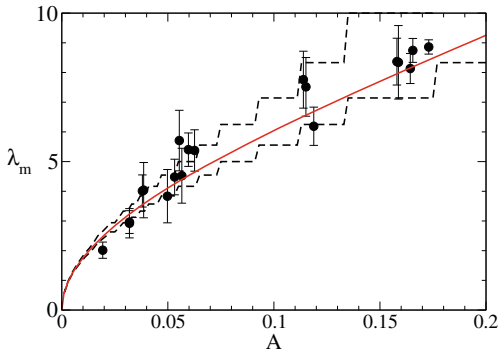

Fig. 6 Average spacing between drops (symbols) as a function of the cross section of the filament, A. The *curve* corresponds to λ_m as predicted by the LSA using $\ell = 10^{-3}$. The step-like *dashed lines* illustrates the finite-size effects, as discussed in the text

one drop with respect to L/λ_m. This leads to the following upper and lower bounds

$$(\lambda_+, \lambda_-) = \begin{cases} \left(\frac{L}{n_0}, \frac{L}{n_0+2}\right) & \text{if } n_d - n_0 > 0.5 \\ \left(\frac{L}{n_0-1}, \frac{L}{n_0+1}\right) & \text{if} n_d - n_0 < 0.5, \end{cases} \tag{33}$$

where n_0 is the integer part of L/λ_m. The piecewise staircase function plotted in Fig. 6 shows that most of the experimental data fall within the band of expected values of the spacing. Note that for large areas, the number of drops strongly decreases, and thus the band $(\lambda_+ - \lambda_-)$ increases in size, justifying finding larger dispersion in the experiments.

2.4 Energy Modeling

In this section, we aim to predict the number, size, and distribution of the primary drops in terms of the energy variation between initial and final stages. To do so, we consider the total energy (in units of γ) as

$$E = S - S_w \cos\theta_0 + E_g, \tag{34}$$

where S is the free surface area, S_w is the wetted area (projection of S on the substrate), and E_g is the gravitational energy. We apply this definition to both the initial filament and the resulting final drops.

Since we measure both the diameter, d, of the original jet and the length of the filament on the substrate, L, the initial energy of the system is given by the filament energy, E_f, defined by means of (34). Note that both the jet and captured filament have the same cross section, $A = \pi d^2/4$. Thus, for given A and θ_0, (5)–(9) allow us to calculate s_0, and terms for the energy filament, E_f, are

$$\begin{aligned} S_f &= L\int_0^{s_0} \sqrt{1 + \left(\frac{\partial h_0}{\partial x}\right)^2}\, dx, \quad S_{w,f} = 2s_0 L, \\ E_{g,f} &= L\int_0^{s_0} h_0(x)^2\, dx. \end{aligned} \tag{35}$$

Regarding the final shape of the drops, we simplify our approach by considering that all of them adopt the *spherical cap* shape. Moreover, since the drops are of nearly equal size, we consider that the final system is formed by n equal drops of volume V_d with radius r_d and contact angle θ_0. Then, for given A and θ_0, the drop volume is given by,

$$V_d = \frac{1}{6}\pi r_d^3 (2 + \cos\theta_0) \frac{\tan\theta_0/2}{\cos^2\theta_0/2}, \tag{36}$$

while the energy terms that compose the drop energy, E_d, are

$$\begin{aligned} S_d &= \frac{\pi r_d^2}{\cos^2\theta_0/2}, \qquad S_{d,w} = \pi r_d^2, \\ E_{g,d} &= \frac{1}{12}\pi r_d^4 \left(\frac{1}{\cos^4\theta_0/2} - 1\right). \end{aligned} \tag{37}$$

Since the final stage satisfies $nE_d \leq E_f$, and mass conservation requires, $n = LA/V_d$, we have

$$\frac{E_d}{V_d} \leq \frac{e_f}{A}, \tag{38}$$

where $e_f = E_f/L$ is the energy per unit length of the initial filament. The marginal criterion (equality in this expression) would lead to a prediction of the maximum number of drops, n_0. In principle, the system could evolve to a certain n ($< n_0$), as small as 1 or 2, if the viscous dissipation is large enough. Thus, the energy balance between the initial and final states should include the viscous dissipation in the form,

$$E_f = e_f L = n(E_d + E_\mu), \tag{39}$$

where E_μ is the energy dissipated to form each primary drop. We observe in the experiments that the only detectable flow is localized in the neighborhood of the tips of the filament. As a consequence, we assume that E_μ is mainly due to the motion of the head of the tip (at the initial condition and also after each breakup), and that its main contribution comes from friction against the substrate. Then, we propose

$$E_\mu = \beta\pi r_d^2, \tag{40}$$

where β is a constant to be determined. Thus, the amount of energy dissipated to form a drop is proportional to the area of its footprint. This parameter β is assumed to be independent of the fluid volume in the filament, AL, but might depend on the wettability of the substrate represented by θ_0. Note that this model implies that every drop is generated from equivalent portions of the filament of equal length, λ_e. This means that the frictional force is basically the same for every drop and that there is a geometrical similarity between drops of different sizes (for different n's) which are produced by different straight portions of the filament. Consequently, it is irrelevant to use λ_e or r_d as scales to quantify the amount of viscous dissipation. Note also that β involves the energy dissipation all over the flow evolution, and then

it includes the time scale of the problem, closely related to the value of viscosity μ.

In summary, we expect β to depend on both θ_0 and μ, but be independent of A. Thus, the resulting energy balance can be written as

$$\frac{E_d + E_\mu}{V_d} = \frac{e_f}{A}. \tag{41}$$

Note that, for given θ_0 and β, the left and right hand sides of this equation are functions of r_d and A, respectively. This allows us to calculate the corresponding distance between drops as

$$\lambda_e = \frac{L}{n} = \frac{V_d(r_d)}{A}, \tag{42}$$

since r_d is obtained from (41) for given A.

In Fig. 7, we compare our experimental values for the distance between drops with the predictions of (42) as a function of the cross-sectional area, A, for different values of β. Clearly, the marginal criterium, which corresponds to $\beta = 0$, does not appropriately describe the experimental data. Instead, some amount of viscous dissipation is required, as shown by the curves with $\beta > 0$. We note in passing that by using elliptic instead of circular drops, we obtain the same result. Furthermore, the final state for larger A's, consisting of two or three drops, is reached only after a few days. These very long times are needed to move the fluid a distance of the order of L, which implies a very strong dissipation.

Our experimental results show that the pearling process on partial wetting substrates includes several interesting problems such as the mechanism of the contact line pinch off. The energy model gives a simple but good enough description of the global evolution of the system to the final state. Here, we are considering a final static state as well as the total viscous dissipation. Thus, our approach differs from previous infinite filament linear analysis [35–37]

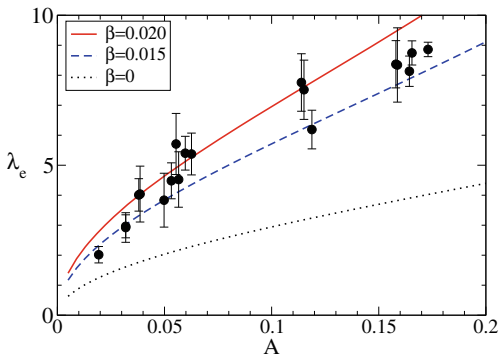

Fig. 7 Comparison of average spacing between drops between experiments (*symbols*) and energy model (*curves*) as a function of the cross section of the filament, A. The *curves* correspond to λ_e for different values of the dissipation coefficient β (see (42))

which are restricted to marginal stability criteria. Note that these are sufficient but not necessary conditions and are independent of viscous dissipation. In our simple model, all the energy lost by viscous effects is embedded in the parameter β. Additional experiments with $\nu = 100\ St$ show that n is independent of viscosity although the time required to reach the final state increases. This suggests that the final pattern is not affected merely by the viscous dissipation rate but by the total dissipated energy. Another possible source of the discrepancy between previous studies on infinite filaments and experimental results lies in the finite nature of the filament which plays an important role in the evolution of the system. Further research is needed to elucidate these issues.

3 Nanometric Range

Now, we focus the analysis of the filament instability in the nanometric range. The experiments described here were performed by the group of Dr. Philip Rack at Center for Nanophase Materials Sciences (Oak Ridge National Laboratory, USA) [38]. In our modeling, we show here that intermolecular forces (of the van der Waals type) have to be included in the formulation and that gravity effects can be safely neglected. Interestingly, the addition of these forces entails the existence of an ultra thin film outside the filament footprint, whose thickness actually depends on the average thickness of the filament itself. At the same time, the inclusion of both attractive and repulsive parts in the intermolecular forces term allows to represent the main partial wetting properties of the fluid.

3.1 Experiments with Liquid Metals

The initial configuration is that of flat filament on a SiO2 substrate. Its definition and deposition were accomplished using electron beam lithography, DC magnetron sputtering, and a solvent facilitated lift-off process, the details of which are provided elsewhere [38]. The total surface array occupied by the filaments on the substrate surface was $\approx 10^5\ \mu\text{m}^2$.

These initially flat filaments (with rectangular cross section) are then irradiated at normal incidence. Since the KrF (248 nm) pulsed laser beam covered a surface area of $\approx 10^7\ \mu m^2$, the relatively larger size of the incident laser pulse ensured that each strip was irradiated with uniform laser fluence. The nanoparticles were performed using (5–10) sequential laser pulses each with a fluence of $180\ mJ/cm^2$. The laser pulse width ($\approx$ 18 ns) was significantly less than the time between pulses (100 ms). This led to non interacting laser pulses, that is, the sample transiently melted, resolidified, and returned to room temperature prior

to the next laser pulse. Moreover, the massive rate of heating and cooling ($\approx 10^8\ K/s$) makes transient phenomena, such as solid-state mass transport and oxidation, negligible. As a result, the total liquid lifetime accumulated using multiple laser pulses leads to the same morphological result as one laser pulse yielding the equivalent liquid lifetime.

3.2 Long Wave Approximation with Disjoining Pressure

In order to describe the dynamics of the liquid filament in the nanometric range, we also use the long wave approximation like in the submillimetric range. We consider now the addition of the long range of intermolecular forces, which are now relevant not only at the contact line region but also on the fluid bulk. The slip model could also be retained here, but for now, we do not include it in this analysis for simplicity. Instead, this model was strictly necessary in the submillimetric case to overcome the contact line singularity.

Thus, the *dimensional* equation that governs the fluid thickness $h(x, y, t)$ is [39]

$$3\mu\frac{\partial h}{\partial t}+\gamma\nabla\cdot\left(h^3\nabla\nabla^2 h\right)+\nabla\cdot\left[h^3\nabla\Pi\right]-\rho g\nabla\cdot\left(h^3\nabla h\right)=0. \tag{43}$$

Here, the first term stands for viscous force, while the other three terms account for the driving forces, namely, surface tension, intermolecular (van der Waals), and gravitational, respectively. The intermolecular force is described by means of the disjoining pressure, Π, which depends on the fluid thickness as,

$$\Pi(h)=\kappa f(h)=\kappa\left[\left(\frac{h_*}{h}\right)^n-\left(\frac{h_*}{h}\right)^m\right], \tag{44}$$

where κ is a characteristic pressure, h_* is an equilibrium thickness, and the exponents satisfy, $n > m > 1$ (note that $f(h)$ is a dimensionless function). The first term in (44) represents the liquid–solid repulsion, while the second term is the attractive part. The balance of both terms leads to a stable film of thickness $h = h_*$, which is related to the precursor film thickness formed ahead of the contact region (see Appendixes A and B in [27]). Within this model, the pressure κ can be written as

$$\kappa=\frac{6\pi\mathcal{A}}{h_*^3}, \tag{45}$$

where $\mathcal{A}$ is the Hamaker constant, which characterizes the intermolecular interaction between the free surface and the substrate surface [27, 40].

By defining the dimensionless variables $\tilde{h}=h/h_*$, $\tilde{x}=x/L_2$, $\tilde{y}=y/L_2$, $\tilde{t}=t/T_2$, with

$$T_2=\frac{3\mu h_*^3}{L_2^4},\qquad L_2=\sqrt{\frac{\gamma h_*}{\kappa}}, \tag{46}$$

(43) becomes

$$\frac{\partial h}{\partial t}+\nabla\cdot\left(h^3\nabla\nabla^2 h\right)+\nabla\cdot\left[h^3 f'\nabla h\right]-B\nabla\cdot\left(h^3\nabla h\right)=0, \tag{47}$$

where $f' = df/dh$ and we have omitted the 'hat' symbol for simplicity. Here, $B = (L_2/a)^2$ is the Bond number. In terms of the atomic distance $\mathcal{D}=\sqrt{\mathcal{A}/\gamma}$, we have

$$L_2=\sqrt{6\pi}\frac{h_*^2}{\mathcal{D}},\qquad B=6\pi\frac{h_*^4}{a^2\mathcal{D}^2}. \tag{48}$$

Typically, $h_* \lesssim \mathcal{D}$ and $\mathcal{D} \ll a$, so that $B \ll 1$, and gravity effects are neglected in nanometric experiments. Then, we will take $B = 0$ in what follows.

3.2.1 Static State (Base) Solution

We first concentrate on the y-independent solution, $h(x, t)$, so that (47) reduces to

$$\frac{\partial h}{\partial t}+\frac{\partial}{\partial x}\left[h^3\left(\frac{\partial^3 h}{\partial x^3}+f'\frac{\partial h}{\partial x}\right)\right]=0. \tag{49}$$

We consider now $\partial h/\partial t = 0$ and look for the static solution $h = h_0(x)$. After integrating twice the resulting equation, and using the symmetry boundary conditions $h_0''' = h_0' = 0$ at $x = 0$, where the primes stand for x-derivatives, we obtain (see, e.g., [27]):

$$h_0''+f(h_0)+p=0, \tag{50}$$

where the constant $p > 0$ is the equilibrium pressure [41, 42] within the fluid. Note that the scale pressure is given by κ. An analysis of the solutions of (50) shows that there is a range of pressures [27, 41, 43]

$$p_{min} < p < p_{max} = \frac{n-m}{n\left(\frac{n}{m}\right)^{m/(n-m)}} \tag{51}$$

for which there exist bounded solutions in which $h_{0,min} < h_0 < h_{0,max}$. The value of p_{min} is related to a drop flattened by gravity, and it is given by:

$$p_{min}=\frac{\rho g a}{\kappa}=6\pi\frac{h_*}{a}\left(\frac{h_*}{\mathcal{D}}\right)^3. \tag{52}$$

Here, we take $p_{min} = 0$, since we neglect gravity effects ($h_* \ll a$) and h_* is of the order of $\mathcal{D}$. On the other hand, both $h_{0,min} \gtrsim 1$ and $h_{0,max}$ depend on the value of pressure, p. The latter also determines the cross section area of the drop, defined as

$$A=2\int_0^\infty\left(h_0(x)-h_{0,min}\right)dx, \tag{53}$$

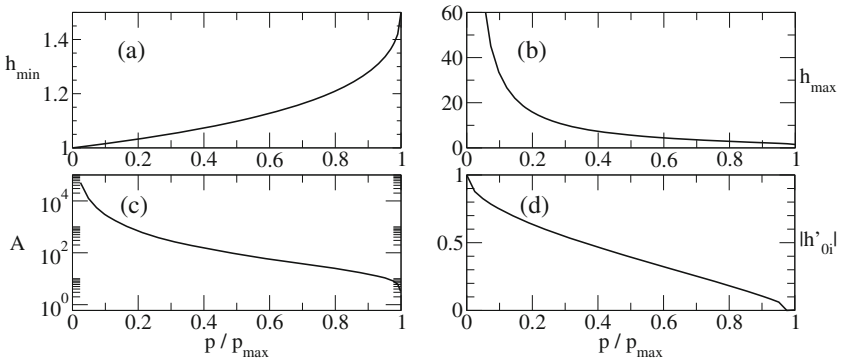

Fig. 8 Static drop parameters as a function of pressure for $(n, m) = (3, 2)$. **a** Minimum thickness (precursor film), **b** maximum thickness (drop height), **d** drop area, **d** slope at the inflection point

where [27, 41] $h_{0,min} \approx h_* + ph_*/(n-m)$. Figure 8 shows the dependence of these variables on p for $(n, m) = (3, 2)$. Note that the precursor film thickness is bounded as [44]

$$1 \leq h_{0,min} \leq \frac{n}{m}, \tag{54}$$

while the maximum drop height satisfies

$$h_{0,max} \geq \frac{n}{2(n-m)}, \tag{55}$$

and increases monotonously as p decreases. Similarly, the area A also increases in a similar fashion. Another parameter of interest is the slope at the inflection point, $h'_{0,i}$, since this is usually defined as the contact angle. It is given by:

$$\tan\theta_i = \frac{h_*}{x_c}\left|h'_{0,i}\right|, \tag{56}$$

Note that the actual contact angle, θ_0, depends on the microscopic parameters, h_* and $\mathcal{A}$, as well as the surface tension, γ. The value of θ_i can be compared with the usual macroscopic contact angle, θ_0, which is estimated assuming a very large ratio $h_{0,max}/h_{0,min}$, i.e., for a drop much thicker than the precursor film (of negligible thickness). This angle θ_0 is related with κ by [45]

$$\kappa = \frac{\gamma\,(1-\cos\theta_0)}{Mh_*}, \tag{57}$$

where $M = (n-m)/[(n-1)(m-1)]$. Substituting into (56), we have

$$\tan\theta_i = \left|h'_{0,i}\right|\sqrt{\frac{2}{M}}\sin\frac{\theta_0}{2}. \tag{58}$$

For $(n, m) = (3, 2)$, we have $\left|h'_{0,i}\right| \to 1$ for $p \to 0$ $(A \to \infty)$, so that we find $\theta_i \to \theta_0$ in the limit of small contact angles. Otherwise, (58) shows the general relationship between both angles.

Figure 9 shows the thickness, slope, and curvature profiles for $p/p_{max} = 0.05$. Note that the slope increases almost linearly up to the inflection point, and then abruptly decreases to zero to meet the precursor film. Also, the negative and uniform curvature in most of the drop volume becomes positive and very large beyond the inflection point and finally goes to zero at the contact region.

3.2.2 Linear Stability Analysis (LSA)

In order to perform the linear stability analysis of the transverse thickness profile, $h_0(x)$, with respect to longitudinal perturbations (y-direction), we write:

$$h(x, y, t) = h_0(x) + \epsilon\chi(x)\exp(\omega t + iky) \tag{59}$$

where ϵ is small number, $\chi(x)$ is the amplitude of the perturbation, $k = 2\pi/\lambda$ is the wave number, and λ is the wavelength.

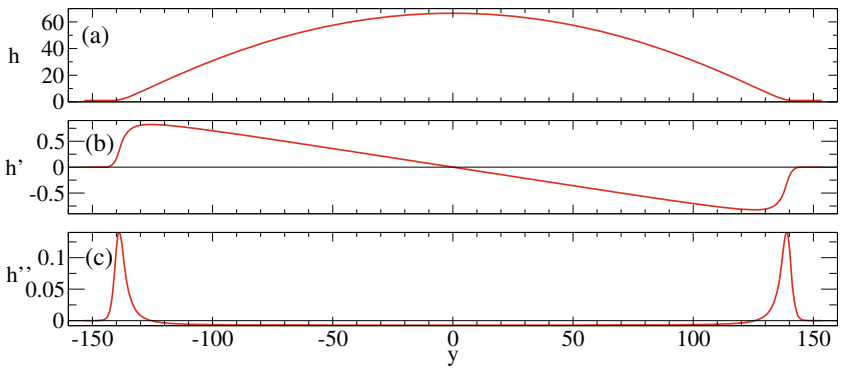

Fig. 9 Profiles of **a** thickness, **b** slope, and **c** curvature of a filament cross section for $p/p_{max} = 0.05$, in which $h_{0,min} = 1.00758$, $h_{0,max} = 66.49$ and $A = 11876.9$

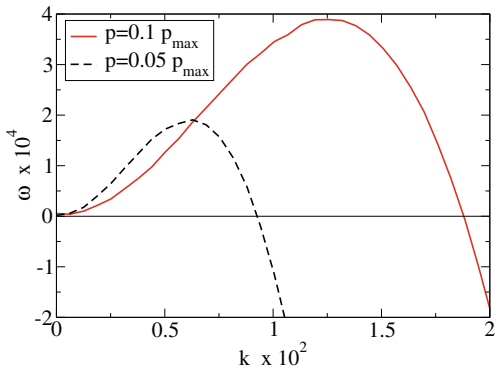

Fig. 10 Dispersion relations, ω versus k, for two values of the fluid pressure, p/p_{max}: 0.1 and 0.05. These cases correspond to the filament cross sections, $A = 2899.3$ and $A = 11876.8$, respectively

By replacing (59) into (49), we obtain to $O(\epsilon)$ the eigenvalue problem:

$$\mathcal{L}\chi = -\omega\chi$$

where $\mathcal{L}$ is the linear operator defined by:

$$\mathcal{L}\chi = c_4(x)\chi_{xxxx} + c_3(x)\chi_{xxx} + c_2(x)\chi_{xx} + c_1(x)\chi_x + c_0(x)\chi, \tag{60}$$

where the coefficients $c_i(x)$ $(i = 0, ..., 4)$ are defined by:

$$\begin{aligned} c_4(x) &= h_0^3, \\ c_3(x) &= 3h_0^2 h_0', \\ c_2(x) &= -\left(1 + 2k^2 - f'\right) h_0^3, \\ c_1(x) &= -h_0^2 \left[3(1 + k^2 - f') - 2h_0 f''\right] h_0' \\ c_0(x) &= c_{0,2} h_0^2 + c_{0,3} h_0^3 + c_{0,4} h_0^4 \end{aligned} \tag{61}$$

and $c_{0,j}$ $(j = 2, 3, 4)$ are given by:

$$\begin{aligned} c_{0,2}(x) &= 3h_0'^2 f'', \\ c_{0,3}(x) &= k^2 \left(1 + k^2 - f'\right) - f''(p + f) + h_0'^2 f''' \\ c_{0,4}(x) &= f'' \end{aligned} \tag{62}$$

Figure 10 shows the resulting dispersion relation curves. We see that the maximum growth rate, ω_m, as well as its corresponding wavenumber, k_m, diminishes as p is decreased (i.e., as A is increased).

3.3 Comparison with Experiments: Melted Metals

The objective of this methodology is to organize an array of nanoparticles originating from the dewetting of a liquid filament. This, however, requires the creation of the semicylindrical filament which is difficult by standard nanolithography. Instead, a very thin flat filament (with rectangular cross section) is deposited and designed to retract upon melting into the desired nanoscale filament geometry. Nanolithography along with physical vapor deposition is used to define metallic (nickel, Ni) thin film filaments with straight edges and length, L. The cross-sectional area of the thin film filament is rectangular with thickness, H, and width, w. When melted, it contracts into a truncated liquid filament of radius, R, according to the following area balance

$$A = Hw = R^2 \left(\theta_0 - \frac{\sin 2\theta_0}{2}\right) \tag{63}$$

where θ_0 is the equilibrium contact angle between the liquid Ni filament and silicon substrate. Thus, the filament morphology results from the conversion of the thin film filament into a liquid by nanosecond pulsed laser induced dewetting (PLiD).

The straight edged filaments of width, w, shown in Fig. 11a, were designed to self-assemble as a filament (with cross section defined by an arc of a circle) by a dewetting process. Figure 11a shows the liquid filament with a radius $R = D/2 = 165 \pm 9\ nm$ which results following five KrF laser pulses with wavelength 248 nm and energy density 420 mJ/cm^2 (liquid lifetime: $5 \times 14.9\ ns = 74\ ns$). An ultra thin reaction layer forms simultaneously during retraction, which is presumably a very thin silicide ($Ni?_x\ Si_y$). This layer conveniently imprints the original footprint of the filament. Then, the out-of-plane capillary forces drive the indicated (yellow arrows) edge and vertex retraction [46, 47].

The brief liquid lifetime per pulse (which can typically go from 7.5 to 14.9 ns) produced during PLiD is of

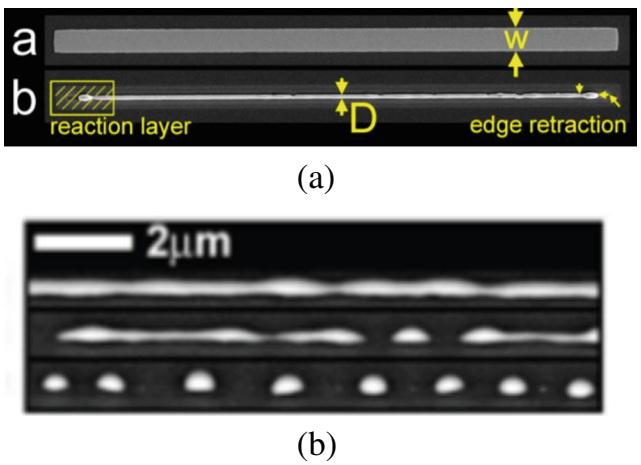

Fig. 11 **a** *Top*: Scanning electron microscopy (SEM) image of a Ni thin film filament following electron beam lithography and metallization. The image was acquired normal to the Si substrate surface, and the filament dimensions are $h_0 = 23 \pm 1.2$ nm, $w = 2.05\ \mu m \pm 18$ nm, and $L = 50 \mu m$. *Bottom*: Flat filaments rapidly transform, by fluid retraction (dewetting), into a rounded filament upon pulsed laser melting. **b** Time evolution of the filament. The scale bars have deliberately been set to equal the fastest growing mode as predicted by LSA. The nanoparticle pitch closely reflects this value

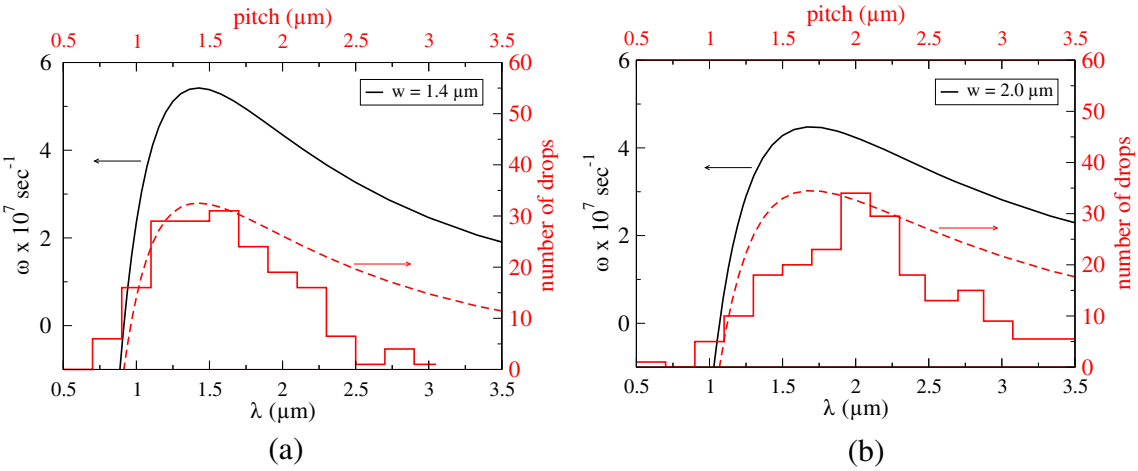

Fig. 12 Dispersion relations, $\omega(\lambda)$, obtained from LSA for $h_0 = 23$ nm (*black solid lines*) for **a** $w = 1.4\ \mu m$ and **b** $w = 2.0\ \mu m$. The corresponding experimental histograms (at right axes in (**a**) and (**b**)) show the number of droplets separated by distances grouped in bins of 200 nm. These histograms are compared with the shapes (*red dashed lines*) of the dispersion relations shown by the *black solid lines*

the same order of magnitude as both the fluid dewetting [46, 48] and the instability time scales [32, 49–51], which govern the filament self-assembly process and nanoparticle breakup, respectively. This convergence of time scales, coupled with the rapid heating and cooling rates, made it possible to capture and visualize the temporal dynamics of the morphology evolution by repetitively pulsing and electron imaging. The filament breakup occurs at the troughs of a varicose instability, as shown in Fig. 11b.

As a result, we obtain the final nanoparticle spacing in the form of histograms as shown in Fig. 12. They count the number of droplets separated by distances grouped in bins of size 200 nm. Interestingly, these distributions mirror quite well the corresponding dispersion curves (ω versus λ) as given by the LSA. This comparison reveals a strong correlation between the LSA predicted perturbation growth rates and the final nanoparticle spacing (pitch). In other words, the wavelengths with greater growth rates correspond to the more frequent particle spacings found in the experiments. Unfortunately, the growth rates themselves cannot be compared since the drops are formed in just a few laser pulses. However, the comparison reveals that the LSA developed here predicts a value of λ_m, the wavelength with maximum growth rate, in good agreement with the most likely distance between drops in the experiment. This is an encouraging result for a continuum theory applied to nanoscales.

4 Summary and Conclusions

We have reported here experiments as well as their corresponding linear stability analyses of a single film configuration, namely a liquid filament on a solid substrate under partial wetting conditions. This has been done in two completely different scales, almost six order of magnitude apart: millimetric and nanometric ones. In spite of this large difference, the comparisons between the experimental data and the hydrodynamical modeling of the problem are highly satisfactory in both scales. This suggests that the conservation laws of the continuum approach are strong enough to allow for a an accurate description of the physical problem provided reasonable assumptions are made on the main driving forces in the problem.

Acknowledgments A.G.G. and J.A.D. acknowledge support from Consejo Nacional de Investigaciones Científicas y Técnicas de la República Argentina (CONICET, Argentina) with grant PIP 844/2011 and Agencia Nacional de Promoción de Científica y Tecnológica (ANPCyT, Argentina) with grant PICT 931/2012.

References

1. I.M.L. Billas, A. Chatelain, W.A. Deheer, Magnetism from the atom to the bulk in iron, cobalt, and nickel clusters. Science **265**, 1682 (1994)
2. Z. Zhang, J.C. Li, Q.J. Jiang, Modelling for size-dependent and dimension-dependent melting of nanocrystals. Q. J. Phys. D: Appl. Phys. **33**, 2653 (2000)
3. A.P. Alivisatos, Perspectives on the physical chemistry of semiconductor nanocrystals. J. Phys. Chem. **100**, 13226 (1996)
4. A.Z.J. Moshfeg, Nanoparticle catalysts. J. Phys. D: Appl. Phys. **42**, 233001 (2009)
5. M.J. Beliatis, N.A. Martin, E.J. Leming, S.R.P. Silva, S.J. Henley, Laser ablation direct writing of metal nanoparticles for hydrogen and humidity sensors. Langmuir **27**, 1241 (2011)
6. B.R. Cuenya, Synthesis and catalytic properties of metal nanoparticles: Size, shape, support, composition, and oxidation state effects. Thin Solid Films **518**, 3127 (2010)
7. H.A. Atwater, A. Polman, Plasmonics for improved photovoltaic devices. Nat. Mater. **9**, 205 (2010)

8. H. Krishna, N. Shirato, C. Favazza, R. Kalyanaraman, Gold nanoparticle array formation on dimpled ta templates using pulsed laser-induced thin film dewettin. J. Mat. Res. **26**, 154 (2011)
9. S.J. Henley, M.J. Beliatis, V. Stolojan, S.R.P. Silva, Gold nanoparticle array formation on dimpled ta templates using pulsed laser-induced thin film dewetting. Nanoscale **5**, 1054 (2013)
10. A.G. González, J. Diez, R. Gratton, J. Gomba, Rupture of a fluid strip under partial wetting conditions. Europhys. Lett. **77**, 44001 (2007)
11. A.G. González, J. Diez, J. Gomba, R. Gratton, L. Kondic, Spreading of a thin two-dimensional strip of fluid on a vertical plane: experiments and modeling. Phys. Rev. E **70**, 026309 (2004)
12. A. Oron, S.H. Davis, S.G. Bankoff, Long-scale evolution of thin liquid films. Rev. Mod. Phys. **69**, 931 (1997)
13. L.W. Schwartz, R.R. Eley, Simulation of droplet motion on low-energy and heterogeneous surfaces. J. Colloid Interface Sci. **202**, 173 (1998)
14. L.W. Schwartz, R.V. Roy, R.R. Eley, S. Petrash, Simulation of droplet motion on low-energy and heterogeneous surfaces. J. Colloid Interface Sci. **234**, 363 (2001)
15. K.B. Glasner, Spreading of droplets under the influence of intermolecular forces. Phys. Fluids **15**, 1837 (2003)
16. L.M. Pismen, Y. Pomeau, Disjoining potential and spreading of thin liquid layers in the diffuse-interface model coupled to hydrodynamics. Phys. Rev. E **62**, 2480 (2000)
17. L.M. Pismen, B.Y. Rubinstein, Spreading of a wetting film under the action of van der waals forces. Phys. Fluids **12**, 480 (2000)
18. J.M. Davis, S.M. Troian, On a generalized approach to the linear stability of spatially nonuniform thin film flows. Phys. Fluids **15**, 1344 (2003)
19. L.M. Pismen, U. Thiele, Asymptotic theory for moving droplet driven by a wettability gradient. Phys. Fluids **18**, 042104 (2006)
20. C.A. Perazzo, J. Gratton, Navier-stokes solutions for parallel flow in rivulets on an inclined plane. J. Fluid Mech. **507**, 367 (2004)
21. R. Goodwin, G.M. Homsy, Viscous flow down a slope in the vicinity of a contact line. Phys. Fluids A **3**, 515 (1991)
22. A. Münch, B. Wagner, Contact-line instability of dewetting thin films. Physica D **209**, 178 (2005)
23. J.H. Snoeijer, Free-surface flows with large slope: beyond lubrication theory. Phys. Fluids **18**, 021701 (2006)
24. G.J. Hirasaki, S.Y. Yang, Dynamic contact line with disjoining pressure, large capillary numbers, large angles and pre-wetted, precursor, or entrained films. Contact Angle, Wettability and Adhesion **2**, 1–30 (2002)
25. L.W. Schwartz, R.R. Eley, Simulation of droplet motion of low-energy and heterogenous surfaces. J. Colloid Interface Sci. **202**, 173 (1998)
26. L.W. Schwartz, R.V. Roy, R.R. Eley, S. Petrash, Simulation of droplet motion on low-energy and heterogeneous surfaces. J. Colloid Interface Sci. **234**, 363 (2001)
27. J. Diez, L. Kondic, On the breakup of fluid films of finite and infinite extent. Phys. Fluids **19**, 072107 (2007)
28. L.M. Hocking, Sliding and spreading of thin two-dimensional drops. Q. J. Mech. Appl. Math. **34**, 37 (1981)
29. E. B. Dussan V., The moving contact line: the slip boundary condition. J. Fluid Mech. **77**, 665 (1976)
30. L.M. Hocking, Spreading and instability of a viscous fluid sheet. J. Fluid Mech. **221**, 373 (1990)
31. L.M. Hocking, M.J. Miksis, Stability of a ridge of fluid. J. Fluid Mech. **247**, 157 (1993)
32. K. Sekimoto, R. Oguma, K. Kawasaki, Morphological stability analysis of partial wetting. Ann. Phys. **176**, 359 (1987)
33. J.P. Boyd, *Chebyshev and Fourier Spectral Methods* (Dover, New York, 2000)
34. J. Diez, A.G. González, L. Kondic, Instability of a transverse liquid rivulet on an inclined plane. Phys. Fluids **24**, 032104 (2012)
35. S.H. Davis, Moving contact lines and rivulet instabilities. Part I: the static rivulet. J. Fluid Mech. **98**, 225 (1980)
36. D. Langbein, The shape and stability of liquid menisci at solid edges. J. Fluid Mech. **213**, 251 (1990)
37. R.V. Roy, L.W. Schwartz, On the stability of liquid ridges. J. Fluid Mech. **391**, 293 (1999)
38. J.D. Fowlkes, L. Kondic, J.A. Diez, Y. Wu, N.A. Roberts, C.E. McCold, P.D. Rack, Parallel assembly of particles and wires on substrates by dictating instability evolution in liquid metal films. Nanoscale **4**, 7376 (2012)
39. J. Diez, A.G. González, L. Kondic, On the breakup of fluid rivulets. Phys. Fluids **21**, 082105 (2009)
40. J.N. Israelachvili, *Intermolecular and surface forces*, second edition (Academic Press, New York, 1992)
41. K.B. Glasner, T.P. Witelski, Coarsening dynamics of dewetting films. Phys. Rev. E **67**, 016302 (2003)
42. A.L. Bertozzi, G. Grün, T.P. Witelski, Dewetting films: bifurcations and concentrations. Nonlinearity **14**, 1569 (2001)
43. K.B. Glasner, T.P. Witelski, Collision versus collapse of droplets in coarsening of dewetting thin films. Physica D **209**, 80 (2005)
44. J.M. Gomba, G.M. Homsy, Analytical solutions for partially wetting two-dimensional droplets. Langmuir **25**, 5684 (2009)
45. M.H. Eres, L.W. Schwartz, R.V. Roy, Fingering phenomena for driven coating films. Phys. Fluids **12**, 1278 (2000)
46. J.D. Fowlkes, Y.Y. Wu, P.D. Rack, Bimetallic nanoparticles by pulsed-laser-induced dewetting: a unique time and length scale regime. ACS Appl. Mater. Interfaces **2**, 2153 (2010)
47. J.H. Snoeijer, N. Le Grand-Piteira, L. Limat, H.A. Stone, J. Eggers, Cornered drops and rivulets. Phys. Fluids **19**, 042104 (2007)
48. P.D. Rack, Y.F. Guan, J.D. Fowlkes, A.V. Melechko, M.L. Simpson, Pulsed laser dewetting of patterned thin metal films: a means of directed assembly. Appl. Phys. Lett. **92**, 223108 (2008)
49. F. Brochard-Wyart, C. Redon, Dynamics of liquid rim instabilities. Langmuir **8**, 2324 (1992)
50. L. Kondic, J. Diez, P. Rack, Y. Guan, J. Fowlkes, Nanoparticle assembly via the dewetting of patterned thin metal lines: understanding the instability mechanism. Phys. Rev. E **79**, 026302 (2009)
51. Y. Wu, J.D. Fowlkes, P.D. Rack, J.A. Diez, L. Kondic, On the breakup of patterned nanoscale copper rings into droplets via pulsed-laser-induced dewetting: competing liquid-phase instability and transport mechanisms. Langmuir **26**, 11972 (2010)